The Planetary Science Journal, 6:111 (20pp), 2025 May https://doi.org/10.3847/PSJ/adccb6

Continental Orientation and the Climate of Land-dominated, Arid Planets

Donald M. Glaser[1,2], Igor Aleinov[1,3], Anthony Leboissetier[1,4], and M. J. Way[1,5]
[1] NASA Goddard Institute of Space Studies, 2880 Broadway, New York, NY, USA; donnymglaser@gmail.com
[2] Blue Marble Space Institute of Science, USA
[3] Columbia University Center for Climate Systems Research, 2880 Broadway, New York, NY, USA
[4] Autonomic Integra, USA
[5] Theoretical Astrophysics, Department of Physics and Astronomy, Uppsala University, Uppsala, SE-75120, Sweden
Received 2024 October 22; revised 2025 March 27; accepted 2025 April 8; published 2025 May 16

Abstract

The climate and habitability of exoplanets are particularly difficult to constrain due to a lack of planetary information (e.g., obliquity and rotation rate) alongside current observational limitations. Surface water content is one of the most highly sought variables given its connections to the origins of life on Earth. Unfortunately, surface water is impossible to constrain due to uncertainties in (i) water content observations and (ii) surface–mantle water differentiation. Global ocean scenarios are prevalent in the literature, but it is vital to investigate the alternative arid scenarios with varied continental orientations and surface water abundances. Here, we use an ensemble of ROCKE-3D global climate model simulations to investigate the potential habitability of single-continent, land-dominated planets. This ensemble simulates climate over a range of water surface areas (WSAs; global ocean coverage) and continental orientations (pole- and equator-centered continents). We find that pole-centered orientations are 2°C–5°C warmer than equator-centered orientations across most WSAs due to the lack of highlands in the northern pole preventing snow and ice accumulation. These differences between continental orientations are completely diminished under the most arid scenarios. This is due to water limitation that results in a breakdown of the ice-albedo feedback, causing warming. Our results show that both WSA and continental orientation play roles in the global mean surface temperature of exoplanets. Future direct imaging missions, such as the Habitable Worlds Observatory, will play a crucial role in constraining the climate of exoplanets due to their ability to assess surface water and land dichotomies.

Unified Astronomy Thesaurus concepts: Habitable planets (695); Planetary atmospheres (1244); Exoplanet surface composition (2022)

Materials only available in the online version of record: figure set

1. Introduction

The search for habitable worlds outside our solar system is a huge endeavor encompassing many disciplines from astronomy and physics to geology and atmospheric science. Several Earth-sized exoplanets in their star's habitable zone (HZ) have recently been discovered (G. Anglada-Escudé et al. 2016; N. Astudillo-Defru et al. 2017; M. Gillon et al. 2017; E. A. Gilbert et al. 2020; L. Delrez et al. 2022; D. Kossakowski et al. 2023; A. Suárez Mascareño et al. 2023, among others); however, observational constraints make the prediction of surface temperature difficult (B. V. Rackham et al. 2018; A. R. Iyer & M. R. Line 2020). In addition, there are too many unknown planetary variables (e.g., obliquity, eccentricity, rotation rate, atmospheric pressure, greenhouse gas abundance, etc.) to constrain surface temperatures with any certainty. Many researchers (e.g., J. Yang et al. 2019; M.-P. Labonté & T. M. Merlis 2020; D. Galuzzo et al. 2021; D. E. Sergeev et al. 2022) have used simplifying approaches to roughly constrain surface conditions, most notably by assuming the most simplistic topography: an aquaplanet (i.e., a planet with a global ocean). This simplifying assumption has provided many benefits to the exoplanet habitability community; however, it has become increasingly necessary to consider more realistic topography scenarios with oceans and land, especially land with relief.

The presence of surface oceans (or land) on an exoplanet is virtually impossible to determine with current technology. The density, and resulting bulk water content, of an exoplanet can be inferred from mass and radius observations, but there are several confounding issues. First, the mass and radius measurements (especially mass) have high uncertainty (S. L. Grimm et al. 2018; C. T. Unterborn et al. 2018). Even with perfectly accurate and precise measurements, water content estimation is highly model-dependent, and there are many degeneracies leading to a wide range of estimations (C. Dorn et al. 2018). The degeneracies stem, primarily, from the unconstrained mass fraction of the core and mantle. There have been attempts to resolve these degeneracies; however, there are still high levels of uncertainty in bulk water content (C. Dorn & T. Lichtenberg 2021; P. Baumeister & N. Tosi 2023). An added layer of degeneracy is introduced when trying to account for water partitioning between mantle and surface (C. M. Guimond et al. 2023). These uncertainties highlight the importance of investigating the large parameter space of surface water inventory to assess the potential climate scenarios within the range of observational uncertainty.

Water-rich exoplanets (aquaplanets or water worlds) with abundant surface water may not be as clement, or conducive to life, as is hoped. The lack of subaerial continents prevents the climate-stabilizing carbonate-silicate cycle (J. C. G. Walker et al. 1981). This cycle is a negative feedback on Earth's

climate that stabilizes clement surface conditions over geologic timescales. The absence of this cycle may lead the planet into a runaway greenhouse (or snowball) state, depending on instellation. The search for habitable surface conditions is ultimately driven by the search for life. Life on Earth is a complex, interconnected system dependent on a relatively narrow range of abiotic factors (J. F. Kasting & D. Catling 2003; S. R. Kane et al. 2019; C. S. Cockell et al. 2024; M. Styczinski et al. 2024). One such abiotic factor, phosphorus, is sourced on modern Earth primarily through the subaerial weathering of continents (L. Noack et al. 2017; D. M. Glaser et al. 2020; D. Höning & T. Spohn 2023). The lack of subaerial continents on an aquaplanet may severely inhibit the development of a large biosphere such that any such biosphere may be undetectable (S. Maruyama et al. 2013; L. Noack et al. 2017). Therefore, the search for life may be the most fruitful in the most arid planets. Counterintuitively, Earth is ∼0.23% water by mass, which is an order of magnitude lower than the best-case uncertainty of exoplanet water content estimations, meaning that Earth's water content cannot be confidently measured on an exoplanet (P. Baumeister & N. Tosi 2023). Therefore, the most Earth-like exoplanets are those planets that are "observationally arid" (L. Noack et al. 2017; D. M. Glaser et al. 2020). These "observationally arid" planets are likely to have some combination of oceans and land on the surface, which supports stable climates and the liberation of bioessential nutrients.

Alternatively, the climate of arid planets has been extensively studied, particularly in M dwarf systems (J. Leconte et al. 2013; K. Menou 2013; D. D. B. Koll & D. S. Abbot 2016; M. Turbet et al. 2016; R. K. Kopparapu et al. 2017; A. J. Rushby et al. 2020; A. H. Lobo et al. 2023), where the planets are likely tidally locked with a permanent dayside and nightside (R. Barnes 2017). The effect of land size, distribution, and orientation, therefore, is particularly important for overall climate as it affects the mean temperature, atmospheric circulation, and ocean circulation in these systems (N. T. Lewis et al. 2018; A. D. Del Genio et al. 2019a; J. Yang et al. 2019; A. M. Salazar et al. 2020; Z. Zhao et al. 2021; E. Macdonald et al. 2022). The surfaces of HZ planets in main-sequence M dwarf systems are thought to be arid. This is due to the high-luminosity, pre-main-sequence phase of M dwarf stars, which can cause runaway greenhouse and eventual atmospheric loss to space (R. M. Ramirez & L. Kaltenegger 2014; R. Luger & R. Barnes 2015; F. Tian & S. Ida 2015). The surface water inventory of terrestrial planets in Sun-like star systems is much more uncertain.

Results from planetary formation simulations show that a high proportion of terrestrial planets in the HZ of a Sun-like star are water-rich and likely have a global ocean (S. N. Raymond et al. 2007; P. S. Zain et al. 2018). However, planetary formation is an extremely complex, stochastic process that has a large range of water inventory outcomes for terrestrial planets in the HZ (D. P. O'Brien et al. 2018). This uncertainty is best exemplified by two areas of ongoing debate: (i) what is the source of Earth's water? (e.g., D. P. O'Brien et al. 2018) and (ii) why is the Earth so dry? (e.g., P. S. Zain et al. 2018; J. Venturini et al. 2020).

There are many intriguing benefits of arid surfaces in the search for habitable environments. The climate of arid planets in Sun-like systems has been shown to be capable of maintaining habitable conditions over a wider range of insolation (compared to aquaplanets) due to their resilience against runaway greenhouse and snowball states (Y. Abe et al. 2011; T. Kodama et al. 2019, 2021).

Here we investigate the potential climate scenarios for an Earth-like, single-continent, land-dominated planet orbiting a Sun-like star. We use a series of climate simulations to investigate the effect of continent orientation and surface water inventory on climate. These simulations, ranging from extremely arid to 50% oceans, explore the underrepresented land-dominated exoplanet climate scenarios. Additionally, we explore the effect of continental orientation within these scenarios to provide further evidence that the orientation—not just the size—of continents has effects on the climate of these planets. Currently, the ocean–land fraction and continental orientation of exoplanets are completely unknown due to technological constraints. However, future exoplanetary missions such as the Habitable Worlds Observatory (HWO; National Academies of Sciences, Engineering, and Medicine 2021; C. K. Harada et al. 2024) may provide necessary constraints on the presence and distribution of land and oceans (e.g., J. H. Jiang et al. 2018). In the meantime (and in preparation for HWO), it is necessary to treat land and ocean distribution as a variable in predictive models, resulting in a range of climate possibilities. These simulations that consider land and ocean are critical to identifying the most promising exoplanet targets for follow-up biosignature observations.

2. Materials and Methods

2.1. ROCKE-3D Global Climate Model

All climate simulations described here were performed using the ROCKE-3D general circulation model, a generalized planetary climate model with heritage from the Goddard Institute for Space Studies modelE climate model (M. J. Way et al. 2017). These simulations use the planet 2.0 branch of the model with an improved surface runoff and dynamic lakes scheme, which provides more accurate simulation of arid climates (K. Tsigaridis et al. 2025). These simulations use 4° latitude by 5° longitude resolution, up to 13 ocean layers (where applicable), 40 atmospheric layers, and a fixed top pressure of 0.1 mbar. Radiative transfer calculations were performed via the coupled SOCRATES package (J. M. Edwards 1996; J. M. Edwards & A. Slingo 1996). These simulations were performed without the presence of prognostic, radiatively active dust or other aerosols.

2.1.1. Planet Parameters

All simulations use the same set of Earth-like planet parameters, including instellation, obliquity, gravity, and surface pressure, among others (Table 1). The atmosphere is N_2-dominated (984 mbar total) with trace CO_2, N_2O, and CH_4 (Table 1). However, to make the results of these experiments more generalizable, we do not include O_2. The star has the same stellar spectrum as the Sun.

All simulations started with the same initial conditions. The initial atmosphere is uniform with regard to both temperature (12°C) and water vapor (0 kg kg^{-1}; i.e., dry). The initial ocean is uniform with regard to temperature (20°C) and salinity (0.035 kg kg^{-1} or 35 psu). The initial soil is uniform with regard to temperature (20°C) and water (0.377 L L^{-1}; i.e., saturated).

The soil is 3.5 m thick with six layers and an impenetrable bottom. Soil water moves between adjacent cells depending on

Table 1
Orbital, Planet, and Atmospheric Parameters

Parameter	Value
Instellation (W m^{-2})	1360.7[a]
Obliquity (deg)	23.44[a]
Eccentricity	0.017[a]
Rotational period (hr)	24[a]
Orbital period (hr)	8760[a]
Radius (km)	6371[a]
Gravity (m s^{-2})	9.807[a]
Surface pressure (mbar)	984[a]
O_2 mixing ratio (ppm)	0
O_3 mixing ratio (ppm)	0
CO_2 mixing ratio (ppm)	285.2[a]
N_2O mixing ratio (ppm)	0.28[a]
CH_4 mixing ratio (ppm)	0.79[a]
CFC mixing ratio (ppm)	0[a]

Note.
[a] Preindustrial Earth values.

topography. Soil texture is an Atacama-like mixture—homogenous with depth—of sand (85%), silt (10%), and clay (5%; D. M. Glaser et al. 2022). The dry soil albedo is 0.2 for wavelengths of 300–4000 nm and uniform for all land cells at model start. The albedo of 0.2 was chosen as an approximation of basalt, similar to the bright regions of Luna (e.g., Tycho; Y. Shkuratov et al. 2011) and the non-Tharsis highlands of Mars (e.g., Noachis Terra; M. Vincendon et al. 2015). The soil texture and albedo were chosen to simulate a minimally weathered, desert-like terrain comprised of primary igneous rock.

2.1.2. Simulation Experimental Variables

Surface topography is one of the primary independent variables in these simulations. Here we use a paleo-Mars (>3.7 Ga; i.e., pre-Tharsis) topography that has been used previously in climate simulations (S. Bouley et al. 2016; S. D. Guzewich et al. 2021). This topography provides an ideal natural laboratory for the study of the effect of land distribution on climate because Mars has a simplistic (yet physically realistic) topography with contiguous highlands and lowlands in roughly 50:50 proportion. This allows us to treat the lowlands as a single ocean basin and the highlands as a single continent (similar to an Earth supercontinent configuration): the most simplistic ocean–land distribution. The simulations consider two topographic scenarios (Figure 1). First, the "original" paleo-Mars topography (Figure 1; top left) is used as a "pole-centered" continental distribution, where the lowland–highland dichotomy is distributed latitudinally and the highlands are centered around the south pole. Second, we create a "equator-centered" continental distribution (Figure 1; top right), where the lowland–highland dichotomy is distributed meridonally and the highlands are centered near the equator. The topography is transformed via a true polar wander (TPW)-like rotation, where the latitude and longitude of the surface topography are rotated about an equatorial axis with respect to the axis of rotation, detailed in Appendix A.

The second primary independent variable is surface water inventory. Here, we determine the ocean–land mask via topography by calculating the necessary sea level height (in 100 m increments) to produce a given water surface area (WSA; 1%, 5%, 10%, 20%, 30%, 40%, and 50% surface area; Table 2 and Table 3). All cells with topography above sea level are land with elevation relative to sea level. All cells with topography below sea level are ocean, with some exceptions for the low water inventory simulations; see Section 2.2. Bathymetry was produced using a pseudo-bathtub approach, where each ocean cell has a minimum depth of 590 m. This is to prevent model crashes that stem from (i) total cell evaporation or (ii) total cell solidification (frozen to the bottom), as the model cannot dynamically change between surface types (i.e., ocean to land). For all ocean cells with a depth greater than 590 m, the depth is set to the bathymetry relative to sea level, up to a maximum depth of 4647 m.

2.2. Low Water Inventory Simulations

The 0% WSA simulations were run under a land planet model configuration, where there are no prescribed bodies of water (oceans or lakes). These simulations were initialized only with saturated soil water, and the water is prognostically distributed over the course of the run into stable surface reservoirs (i.e., lakes).

Additionally, several of the 1% and 5% WSA simulations crashed due to insufficient water volume in ocean cells. In other words, the ocean cells "dried up," which causes the model to irreparably crash. To assess the climate of these low water inventory scenarios, it was necessary to initialize these simulations in the land planet configuration, with no ocean cells. The water in these cases was initialized as lakes, which are capable of complete desiccation. The lake simulations have several differences compared to the ocean simulations, such as no salinity and no "ocean" dynamics. However, these differences had no significant change on the climate, which we describe in detail in Appendix F.

2.3. Control Simulations

Here we compare our ensemble of land-dominated planet simulations to two well-known and well-understood scenarios: modern Earth and an aquaplanet. Both control simulations were run under the same conditions as the test simulations, with the only difference being the land mask (modern Earth continents and 100% surface ocean). This allows us to assess the results of our land-dominated planets within the context of the entire spectrum of WSA.

2.4. Model Output and Postprocessing

Model output data are collected as yearly means of each lat-lon grid cell. The geometric mean of the spatial data is then calculated, producing a 1 yr global mean for each variable of interest.

2.4.1. Cloud Effects

The effects of clouds are of particular interest for this study as clouds are affected by the surface water inventory and therefore play a large role in the overall climate of a planet. The radiative effects of clouds are assessed using two primary model variables: the outgoing top of the atmosphere (TOA) longwave (i.e., thermal) radiation absorbed and reemitted by clouds ($cloud_{lw}$) and the incoming TOA shortwave (i.e., UV–vis)

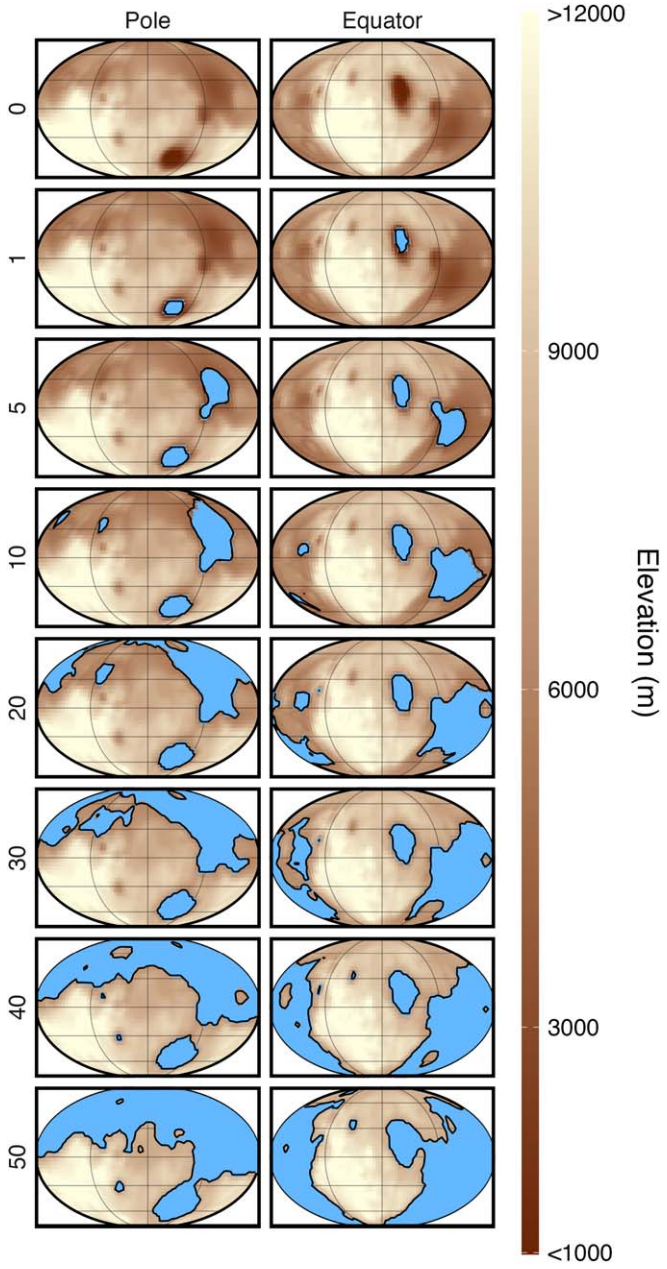

Figure 1. Topography maps as a function of WSA (rows) for the pole-centered (left column) and equator-centered (right column) simulations. Elevation is measured as meters above the lowest point and shown using dark brown as low elevation, light tan as high elevation, and light blue as initial water distribution (ocean or lake). Latitude grid lines are shown at 0°, ±30°, and ±60°.

radiation reflected by clouds (cloud_{sw}). Since clouds have both cooling and warming effects from radiative transfer, it is necessary to calculate the net radiative effect from clouds ($\text{cloud}_{\text{net}}$) as

$$\text{cloud}_{\text{net}} = \text{cloud}_{\text{lw}} - |\text{cloud}_{\text{sw}}|. \quad (1)$$

Incoming cloud_{sw} radiation in the model is negative by convention, so it is necessary to use the absolute value. The calculated $\text{cloud}_{\text{net}}$ shows the net radiative effect, where positive values indicate a net warming effect.

The effect of clouds on planetary albedo can be assessed by proxy using atmospheric albedo,

$$\alpha_{\text{atmos}} = \alpha_{\text{planet}} - \alpha_{\text{ground}}, \quad (2)$$

Table 2
Water Inventory and Corresponding Sea Level for Each Simulation in the Ensemble

WSA (%)	Sea Level (m)	GEL (m)
0	NA	1.1
1	1300	10
5	3700	65
10	4700	140
20	5500	270
30	6100	410
40	6800	640
50	7800	1065

where α_{planet} is the planetary albedo, α_{ground} is the ground albedo, and α_{atmos} is the atmospheric albedo, which includes reflection by clouds and absorption by gas phase constituents (A. Donohoe & D. S. Battisti 2011). To first order, α_{atmos} is dominated by cloud reflection, so we use α_{atmos} as a proxy for the effect of clouds on planetary albedo (G. L. Stephens et al. 2015). Ground and planetary albedo are covered in more detail in Section 3.3.

2.4.2. Assessing Equilibrium

Here we assess the global climate state averaged over 50 yr of equilibrium conditions. We determine equilibrium by first calculating the z-statistic (z) of a given variable over a 50 yr period,

$$z = \frac{m}{se}, \quad (3)$$

where m is the slope of the linear regression and se is the standard error of the regression (C. C. Clogg et al. 1995). The z-statistic is then used to calculate a two-tailed p-value using a normal distribution, comparing the slope (m) to a mean with a slope = 0. If the p-value is greater than or equal to 0.05, the simulation is not significantly changing with time and is considered in equilibrium for that given variable (see Appendix B). The equilibrium climate state is then reported as the mean of the 50 yr subset.

We consider two main categories of variables to assess equilibrium: climatalogical and hydrological. Climatological equilibrium is assessed using two variables: surface temperature (T_{surf}; °C) and the net radiative balance of the planet at the TOA (Rad_{net}; W m^{-2}). T_{surf}, a primary model output, is the air temperature of the atmospheric layer that directly overlies the land or ocean surface. Rad_{net} is a derived variable, calculated using

$$\text{Rad}_{\text{net}} = \text{Rad}_{\text{inc}}(1-\alpha_{\text{planet}}) + \text{Rad}_{\text{out}}, \quad (4)$$

where Rad_{inc} is the incident TOA solar radiation, α_{planet} is the planetary albedo, and Rad_{out} is the outgoing TOA thermal radiation. Positive Rad_{net} values indicate, by convention, that the planet receives more energy than is lost to space.

Hydrological equilibrium is assessed using precipitation (Prec; mm day^{-1}) and potential evaporation (Evap_{pot}; mm day^{-1}). Prec, a primary model output, is the total water precipitation (including snow) onto a land or ocean surface. Evap_{pot} is a derived variable and describes the evaporation that would occur given an infinite source of water and, in brief,

is a function of air density, specific humidity, and wind speed previously described by others (I. Aleinov & G. Schmidt 2006).

3. Results

3.1. Simulation Equilibrium

All simulations ran for at least 550 orbits (1 orbit = 1 Earth yr) and reached climatalogical and hydrological equilibrium according to the methods described in Appendix B (Appendix Figure 9 and corresponding figure set). In addition to climatalogical and hydrological equilibrium, we also assess radiative balance as an indicator of steady-state conditions. Our criteria to assess radiative balance is equilibrium Rad_{net} between -0.3 and $0.3\,W\,m^{-2}$ (Appendix Figure 10), which is more strict than previously described model intercomparison methods (T. J. Fauchez et al. 2020).

3.2. Surface Temperature

Here we present T_{surf} in two different ways: spatial data of a temporal mean (2D map; Figure 2) and a spatial and temporal mean value (single value; Figure 3(A)). In general, these results show a positive trend, for both continental orientations, between WSA and T_{surf}. This trend continues with the aquaplanet and modern Earth control simulations. The 0% and 1% WSA simulations, however, do not follow this trend (Figure 3(A)). The 0% and 1% WSAs, for both continent orientations, are roughly 5°C warmer than the 5% WSA simulations.

The pole-centered simulations are, in most cases, 3°C–5°C warmer compared to the equator-centered simulations. This trend breaks down for the 0% and 1% WSA simulations, where both continent orientations are roughly the same mean global T_{surf}. Additionally, the 20% WSA simulations show little difference in mean global T_{surf} between the continental orientations.

3.3. Albedo

Ground albedo is the reflectivity of a surface, and in these simulations, ground albedo is a mixture of liquid water (albedo ≈ 0.05), land surface (albedo ≈ 0.2), and snow or ice (albedo ≈ 0.8). Equilibrium mean global ground albedo for each simulation is shown in Figure 3(B). Ground albedo and snow and ice coverage are closely correlated, as snow and ice have a high albedo (Figure 3(C)). There is a clear negative trend for both continental configurations in ground albedo as a function of WSA including modern Earth and the aquaplanet (Figure 3(B)). This trend, however, does not hold for the 0% and 1% WSA simulations, as their mean global ground albedo is similar to the 40% and 50% WSA simulations.

In many cases, the equator-centered simulations have slightly higher (3%–5%) ground albedo. This does not hold for the 0%, 1%, and 50% simulations, where the equator-centered simulations have only slightly higher ground albedo, or in the case of the 20% simulation, where the pole-centered simulation has a slightly higher ground albedo.

Planetary albedo is similar to ground albedo but also includes clouds (albedo ≈ 0.5). The equilibrium mean planetary albedo for each simulation is shown in Figure 3(D). There is a negative trend between WSA and planetary albedo, similar to ground albedo; however, the trend is not as strong.

Table 3
Simulation List

Simulation Name	Continental Distribution	WSA (%)	Model Configuration
P.1	Pole-centered	0	Lakes
P.2	Pole-centered	1	Lakes
P.3	Pole-centered	5	Ocean
P.4	Pole-centered	10	Ocean
P.5	Pole-centered	20	Ocean
P.6	Pole-centered	30	Ocean
P.7	Pole-centered	40	Ocean
P.8	Pole-centered	50	Ocean
E.1	Equator-centered	0	Lakes
E.2	Equator-centered	1	Lakes
E.3	Equator-centered	5	Lakes
E.4	Equator-centered	10	Ocean
E.5	Equator-centered	20	Ocean
E.6	Equator-centered	30	Ocean
E.7	Equator-centered	40	Ocean
E.8	Equator-centered	50	Ocean
Earth	NA	71	Ocean
Aqua	NA	100	Ocean

Again, the 0% and 1% simulations are outliers for the negative trend. Similar to ground albedo, the equator-centered simulations have roughly 2% higher planetary albedo compared to the pole-centered simulations with the exception of the 1%, 20%, and 50% simulations.

3.4. Clouds

ROCKE-3D's cloud scheme allows detailed investigation of clouds, and we show global mean cloud coverage (Figure 4) and the net radiative effect from clouds, calculated using Equation (1) (Figure 5 (top panel)). The spatial and vertical extents of the clouds for all simulations are shown in Appendix D (Figures 11 and 12). The 5%–100% WSA simulations have similar total cloud coverage, between 55% and 60%, and the Arrakis-like simulations have between 35% and 40% total cloud coverage (Figure 4). There are no significant differences in total cloud coverage between the continental orientations across all simulations. Low- (>680 mb) and mid- (680–440 mb) altitude clouds do not show a trend with WSA, but there is a marked difference between the 5%–100% and Arrakis-like simulations, similar to total cloud coverage. High-altitude (440–50 mb) clouds show a positive trend with WSA across all simulations. Global mean cloud coverage does not seem to be largely affected by continental orientation, and the only notable difference is in the low-altitude clouds.

In general, there is a negative trend between $cloud_{net}$ and WSA, and most simulations show a net cooling effect from clouds (i.e., negative $cloud_{net}$; Figure 5 (top panel)). The Arrakis-like simulations (0% and 1% WSA), however, show minimal or near-zero $cloud_{net}$ indicating that clouds have little effect on radiative balance in the driest scenarios. The equator-centered simulations have slightly lower $cloud_{net}$ in most cases compared to the pole-centered simulations, indicating a small, $\sim 3\,W\,m^{-2}$, cooling effect from clouds. This $cloud_{net}$ difference between the continental orientations is not evident in the Arrakis-like simulations. Global mean atmospheric albedo (see Equation (2)) shows a positive relationship with WSA across

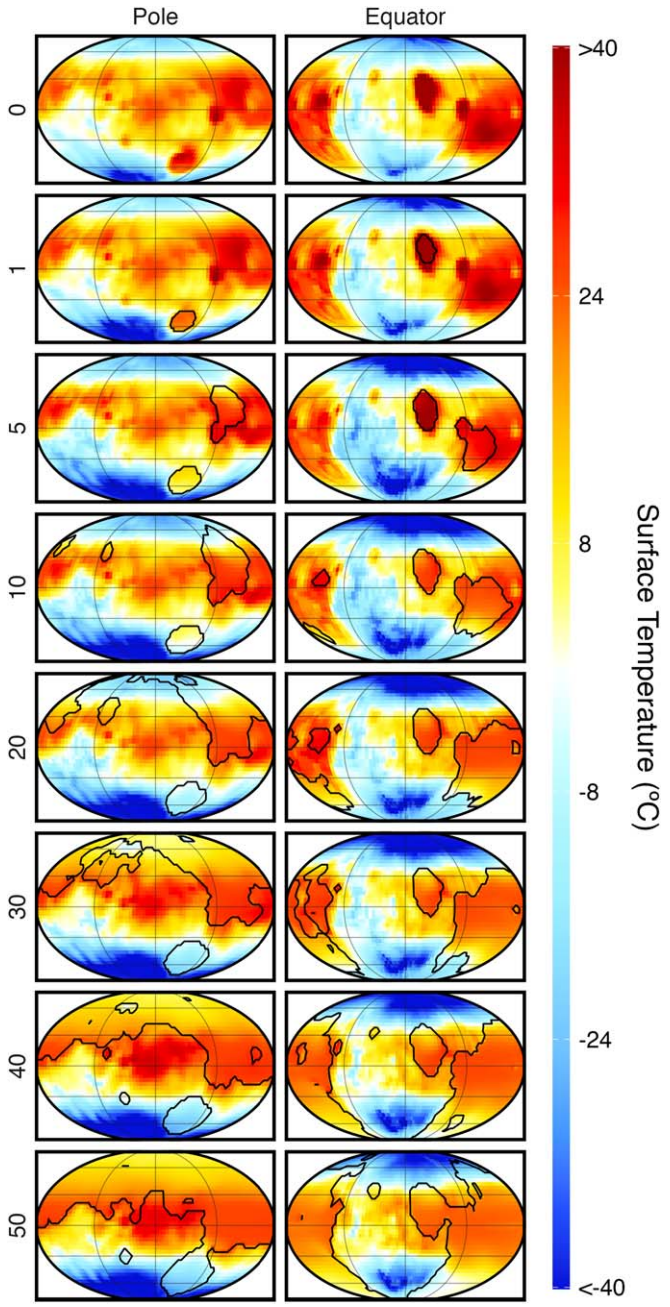

Figure 2. Equilibrium mean annual surface temperature maps as a function of WSA (rows) for the pole-centered (left column) and equator-centered (right column) simulations. The dark black lines are initial sea level, separating land from ocean/lake. Latitude grid lines are shown at 0°, ±30°, and ±60°.

all simulations, as shown in Figure 5 (middle panel). This suggests that increased WSA increases the mean albedo of clouds, even under Arrakis-like conditions. Figure 5 (bottom panel) shows a simple scatter plot between net cloud radiative effects and global mean cloud albedo. Here we observe a distinct negative trend for all simulations and controls.

3.5. Atmospheric and Ocean Circulation

3.5.1. Atmospheric Circulation

We observe changes in atmospheric circulation as a function of both WSA and continental orientation. Figure 6 shows the zonally averaged mean meridional atmospheric circulation for all simulations and controls. In the pole-centered simulations, we observe a strong northern Hadley cell and a weak southern cell at the lowest WSA. The northern cell decreases in magnitude and the southern cell increases in magnitude with increasing WSA until 50% WSA, where the two are similar, at roughly Earth-like magnitude and distribution. Conversely, the equator-centered simulations show a weak northern Hadley cell and a strong southern cell at the lowest WSA. With increasing WSA, the northern cell increases in magnitude while the southern decreases until 50% WSA, where the northern cell is slightly stronger than the southern cell. From 0% to 40% WSA, the pole-centered simulations show a strong northern Hadley cell, with magnitudes greater than all other simulations.

The Arrakis-like simulations show an asymmetry in Ferrel cells. The pole-centered simulations have a prototypical northern Ferrel cell, driven by the strong Hadley cell, but the southern Ferrel cell is weak or nonexistent. The equator-centered simulations show an opposite asymmetry, where the southern Ferrel cell is in typical magnitude and form, but the northern cell is weak or nonexistent.

3.5.2. Ocean Circulation

We observe changes in ocean circulation as a function of both WSA and continental orientation (Figure 7). This is intuitive as increased WSA (and increased ocean volume) allows a greater extent of circulation. Additionally, the pole-centered orientation, at 40% and 50% WSA, has a longitudinally continuous ocean above 30°N. This creates strong currents that circumnavigate the planet, similar to the Southern Ocean on Earth. The equator-centered orientation has no longitudinally continuous ocean at all WSAs, inhibiting ocean circulation.

4. Discussion

4.1. Climatological Differences Due to Water Inventory

Water inventory has been shown previously to have a general warming effect on climate (e.g., M. Turbet et al. 2016; M. J. Way & A. D. Del Genio 2020, among others). This is due to three primary effects: (i) the low albedo of liquid water, (ii) the high heat capacity of liquid water, and (iii) the greenhouse effect of water vapor. A larger aerial extent of oceans (i.e., WSA) increases heat absorption (through albedo) and increases heat retention (through heat capacity). Additionally, the thermal absorption and reemission of water vapor increases surface temperatures. Therefore, for a given solar constant, increased WSA increases the mean global T_{surf} as shown in Figure 3(A).

Arid planets (i.e., extremely water-limited or Arrakis-like), however, do not follow this trend, as has been shown previously by Y. Abe et al. (2011) and M. J. Way & A. D. Del Genio (2020). We consider the 0% and 1% WSA simulations in these experiments to be Arrakis-like. Our results are consistent with these previous findings, where the 0% (1.1 m global equivalent layer, GEL) and 1% (10 m GEL) WSA simulations are warmer than the 5%, 10%, and 20% WSA simulations (Figure 3(A)). Y. Abe et al. (2011) explain that the limited water inventory of Arrakis-like planets prevents snow and ice deposition, maintaining a relatively low ground albedo, causing warming. Our results show similar warming in the Arrakis-like simulations caused by limited snow and ice coverage (Figure 3(C)).

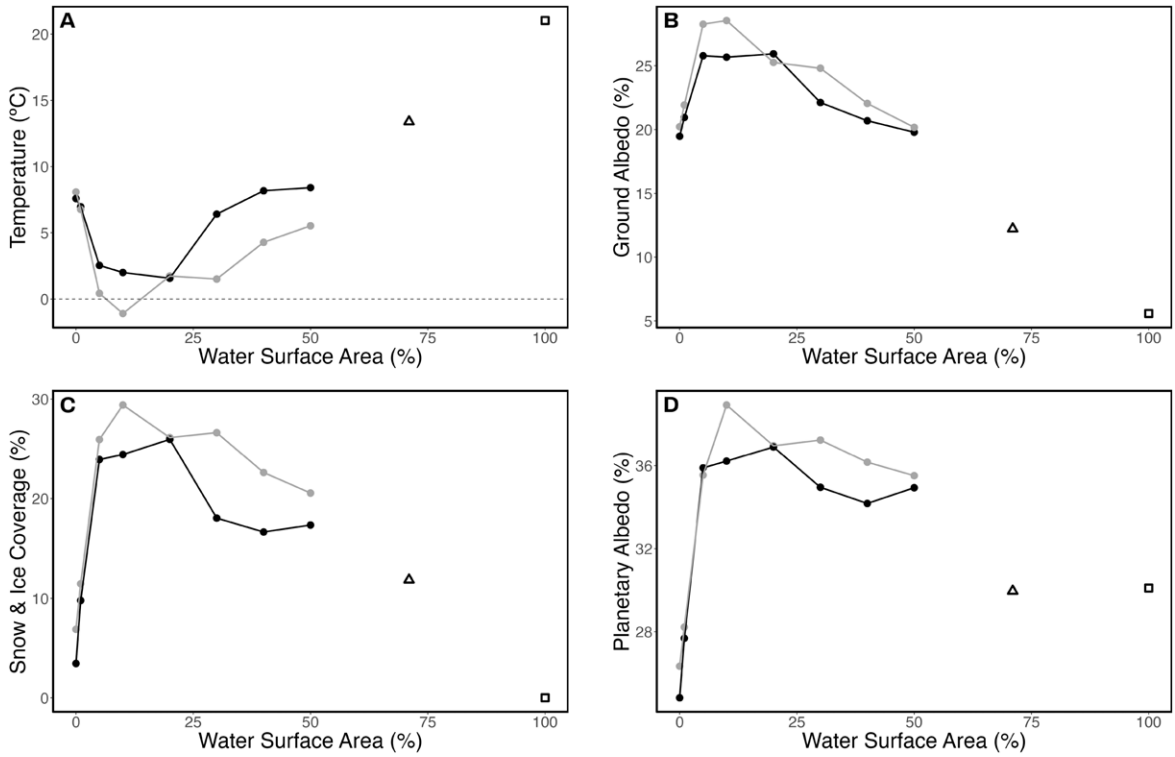

Figure 3. Equilibrium mean global (A) surface temperature, (B) ground albedo, (C) snow and ice coverage, and (D) planetary albedo as a function of WSA for the pole-centered (black) and equator-centered (gray) simulations. Control simulation results for Earth (triangle) and an aquaplanet (square) are shown for comparison. The dashed gray line in panel (A) at 0°C is shown for reference. All variables show a trend (positive in panel (A), negative in (B), (C), and (D)) with WSA between 5% and 100% WSA. The Arrakis-like simulations (0% and 1% WSA), however, do not fit any of the trends. All variables, in most cases, show a notable difference between the pole- and equator-centered continental orientations between 5% and 100% WSA. This difference is muted or eliminated in the Arrakis-like simulations.

Water clouds introduce complexity into this general trend as clouds (sourced from surface water) can have both warming and cooling effects. We show a $\text{cloud}_{\text{net}}$ of roughly 0 for the Arrakis-like scenarios (Figure 5 (top panel)), which works in tandem with reduced snow and ice to create a lower planetary albedo (Figure 3(D)). The balanced $\text{cloud}_{\text{net}}$ negates the cooling effects of clouds seen in the simulations with $\geqslant$5% WSA. The confluence of these factors (lower snow and ice fraction and neutral cloud radiative effects) result in a substantively warmer climate for arid, Arrakis-like planets.

Most observed variables (e.g., T_{surf}, α_{ground}, α_{planet}, total cloud coverage, and $\text{cloud}_{\text{net}}$) show a steplike change between the 0% and 1% WSA and 5% WSA simulations. However, the global mean atmospheric albedo (α_{atmos}; proxy for cloud albedo) shows a continuous, positive trend with WSA (Figure 5 (middle panel)). Similarly, we observe a continuous, negative trend between atmospheric albedo and net cloud radiative effects (Figure 5 (bottom panel)). These two relationships suggest that WSA has a direct effect on atmospheric albedo that increases cooling (via cloud radiative effects). This is true across all simulations in our ensemble and indicates a climate mechanism that behaves similarly across many orders of magnitude of surface water inventory.

Increased water inventory has an effect on the atmospheric circulation: changing both magnitude and distribution (Figure 6). The 50% WSA simulations have Hadley cells that are similar in both magnitude and distribution to Earth. However, the Arrakis-like simulations show unique patterns that manifest in different ways as a function of continental orientation (discussed in Section 4.2.3).

Increased water inventory intuitively has an effect on ocean circulation, which we observe in Figure 7. In general, the magnitude of circulation increases with increasing WSA. This is most evident in the pole-centered simulations that we cover in detail in Section 4.2.3. The clearest evidence for this is in comparison to the aquaplanet simulation, where the stream function magnitudes are $\sim$50 times larger than any of the other simulations.

4.2. Climatological Differences Due to Continental Orientation

The effects of continental orientation on climate, particularly in land-dominated planets around Sun-like stars, are not as well understood, especially in concert with changes in water inventory. This ensemble of experiments was designed to investigate the effects of continental orientation (pole- and equator-centered continents) on climate over a range of water inventory (0%–50% WSA). Our equilibrium mean global T_{surf} results (Figure 3(A)) show clear differences between the two continental configurations from 5% to 50% WSA, with the exception of 20%.

The lower mean global T_{surf} in the equator-centered simulations is due, in part, to increased ground albedo, shown in Figure 3(B). On a spatial scale, this can best be explained by the global distribution of highlands (elevation $>$7800 m), particularly within the high latitudes ($>60°$ or $<-60°$). The equator-centered configuration has $\sim$17% of its highlands in the high latitudes, whereas the pole-centered configuration only has $\sim$12% of its highlands in the high latitudes. Therefore, the abundance of high-latitude highlands lowers the global T_{surf} through high-albedo snow and ice accumulation (see

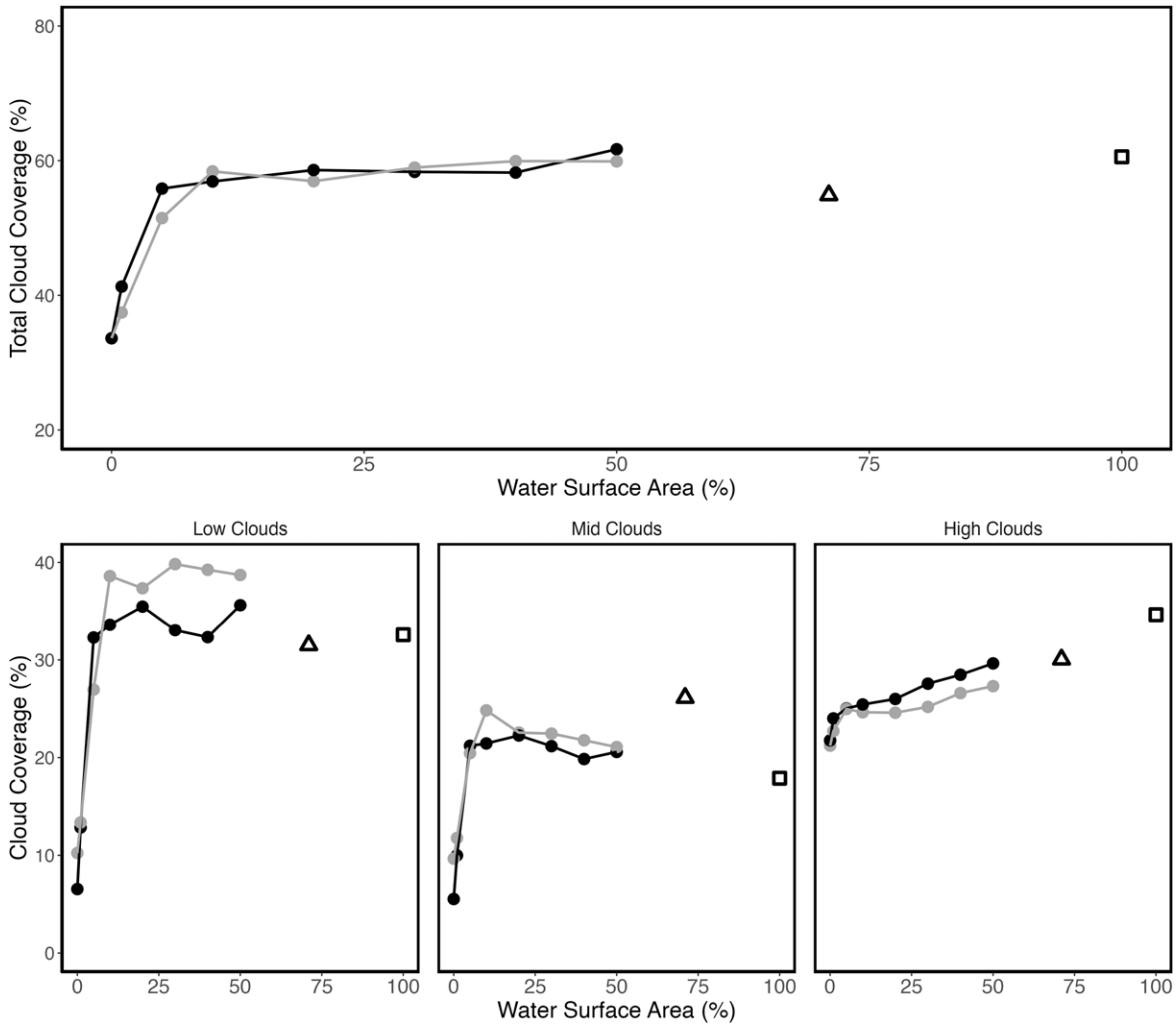

Figure 4. Top panel: equilibrium global mean total cloud cover as a function of WSA. Bottom panels: equilibrium global mean low- (>680 mb), mid- (680–440 mb), and high- (440–50 mb) altitude clouds as a function of WSA. All panels show the pole-centered simulations in black and equator-centered simulations in gray, and the control simulations for the modern Earth (triangle) and aquaplanet (square) are shown for comparison. Total, low-, and midaltitude clouds do not show a trend with WSA, but there is a large difference between the Arrakis-like simulations and the 5%–100% simulations. High clouds, conversely, show a positive relationship with WSA across all simulations including Arrakis-like. Continental orientation only plays a role in low clouds. Note the difference in scale between the top and bottom panels.

Section 4.2.1). The effects of continental configuration on clouds do not have a significant spatial pattern, but the global radiative balance is different between the two configurations.

4.2.1. Snow and Ice Coverage

Figure 8 shows the snow and ice fraction (land, lake, and sea ice) for both orientations of the 1%, 10%, and 50% WSA simulations. The high latitudes of the pole-centered orientations have limited snow and ice in the northern hemisphere. This is due to the fact that 100% of the northern high latitudes are lowlands, which have a mean annual $T_{\text{surf}} \sim 24°\text{C}$ warmer than the equator-centered counterparts (Figure 2). The equator-centered orientations, conversely, have snow and ice on both poles, since both high-latitude regions have highlands. This difference in highland distribution, not just land distribution, explains the disparity in global snow and ice coverage (Figure 3(C)) and plays a role in global T_{surf} (Figure 3(A)).

The spatial disparity between the continental orientations is stark, particularly in the 1% and 50% WSA simulations (Figure 8). The snow and ice caps of the equator-centered orientation serve to cool both poles in the summer, leading to an overall cooler global climate, as similarly shown by M. J. Way et al. (2021). The 1% WSA simulations have an obvious difference in the distribution of snow and ice. However, their global extent is roughly the same. This indicates that the primary factor in snow and ice formation is water limitation, not highland distribution. Therefore, we do not see substantial differences in T_{surf} between the pole- and equator-centered simulations at 1% WSA (Figure 3(A)).

For 10% and 50% WSA, the equator-centered simulations have 20% and 24% more snow and ice coverage, respectively. This disparity in snow and ice coverage leads to differences in T_{surf}. The 10% pole-oriented simulation (P.4) does have some limited snow and ice coverage at the north pole. This is due to an alleviation of water limitation compared to the drier simulations but is still lacking widespread oceans, compared to the wetter simulations, for heat retention.

Ocean circulation and heat transport (see Figure 7) have little to no effect on snow and ice coverage. Figure 7 shows strong

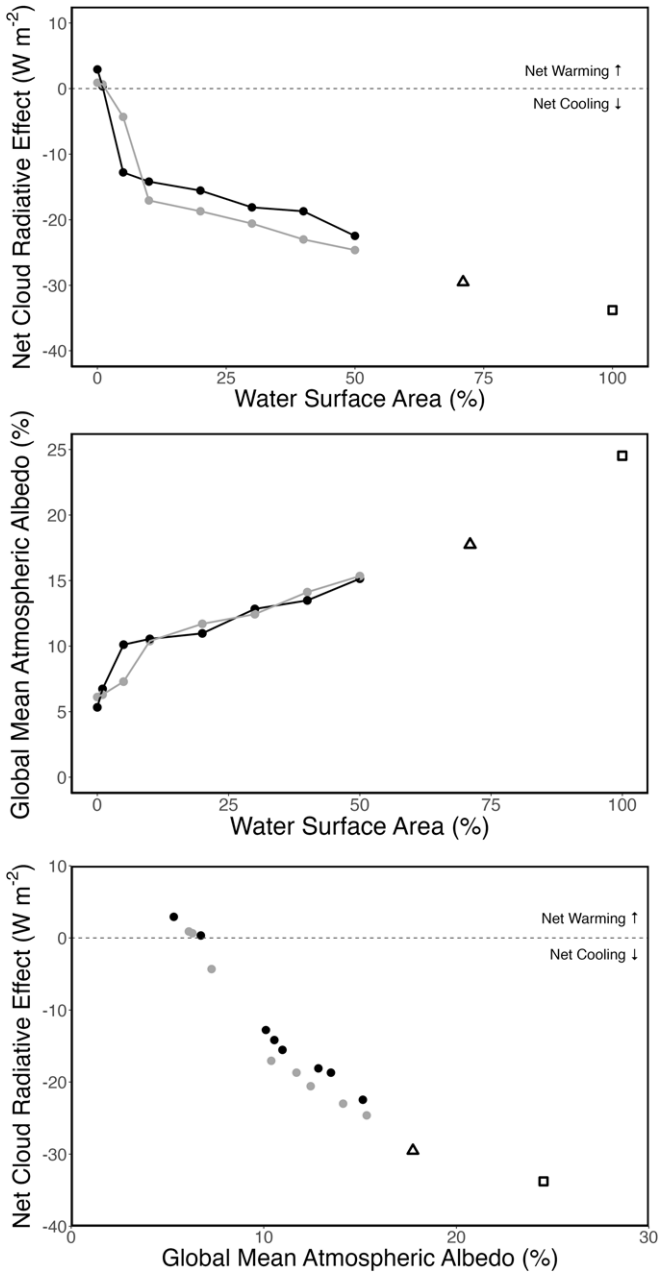

Figure 5. Top: global mean equilibrium net radiative effects from clouds as a function of WSA. Middle: global mean atmospheric albedo as a function of WSA. Bottom: global mean equilibrium net radiative effects from clouds as a function of global mean atmospheric albedo. In all panels, black is the pole-centered and gray is the equator-centered simulations. Control simulations for the modern Earth (triangle) and aquaplanet (square) are shown for comparison. Positive net cloud radiative effect values indicate a net warming effect from clouds. The top panel, between 5% and 100% WSA, shows (i) a negative relationship between $\text{cloud}_{\text{net}}$ and WSA, (ii) net cooling from clouds, and (iii) a minor difference ($\sim$2 W m^{-2}) between continental orientations. The Arrakis-like simulations do not fit the trend, show net zero (or slight warming) from cloud radiative effects, and show less difference between continental configurations. However, the middle and bottom panels both show continuous trends. The negative trend in the bottom panel indicates that the net cooling effect from clouds is dependent on the global mean atmospheric albedo across all WSAs.

ocean circulation for the P.8 simulation, even into the Hellas basin ocean. Despite this circulation and heat transport, there is widespread sea ice in the P.8 simulation (Figure 8). This further supports our assertion that the distribution of land, particularly in the poles, is important to snow and ice coverage and ultimately in overall climate.

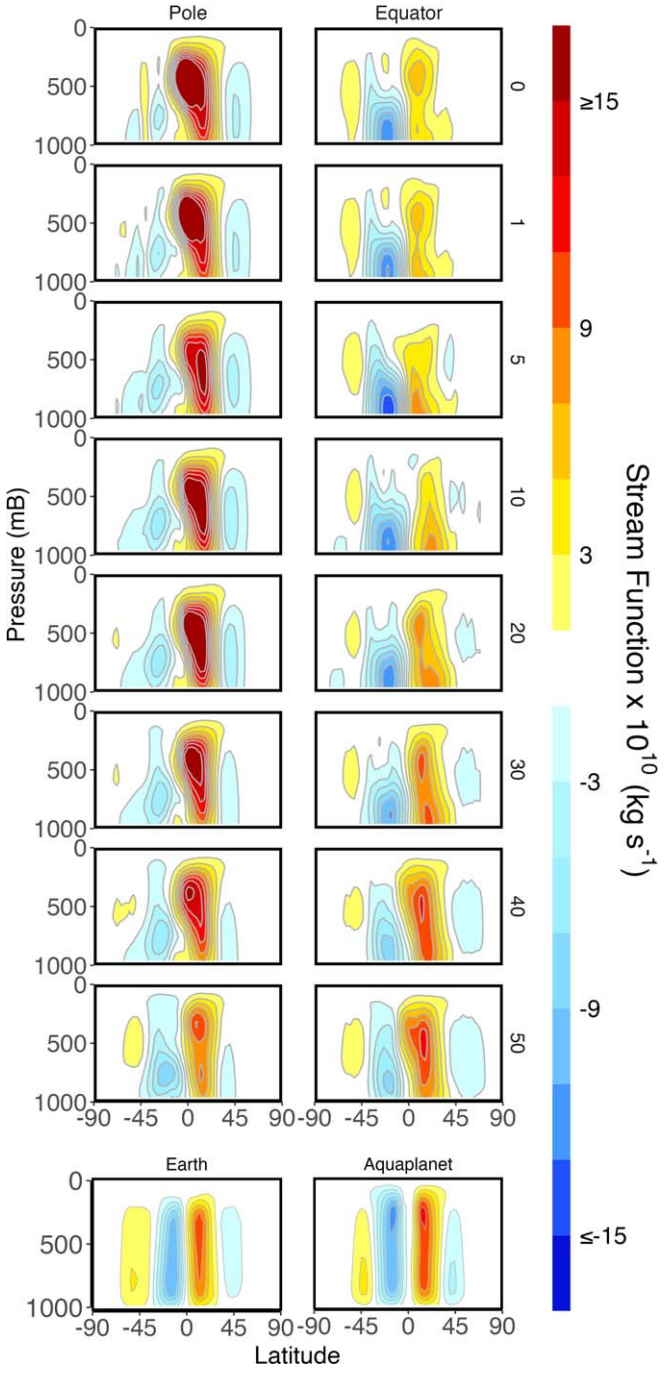

Figure 6. Zonally averaged stream function of the mean meridional circulation as a function of latitude and pressure for all WSA (rows) and both continental orientations (columns). Earth and aquaplanet control simulations are shown on the bottom left and right, respectively, for comparison. By convention, positive stream function values indicate clockwise flow. White values indicate stream function values between -1 and 1×10^{10} kg s^{-1}.

4.2.2. Clouds

Clouds have complex effects on climate as they can cause both cooling and warming. The differences in the $\text{cloud}_{\text{net}}$ between the two continental orientations have the effect of roughly 3 W m^{-2} ($\sim$20%) more cooling from clouds in the equator-centered simulations (Figure 5 (top panel)). This magnitude of cooling holds for all simulations with $\geqslant$10% WSA. The E.3 simulation is the only non-Arrakis simulation that has a lower cooling effect than the pole-centered

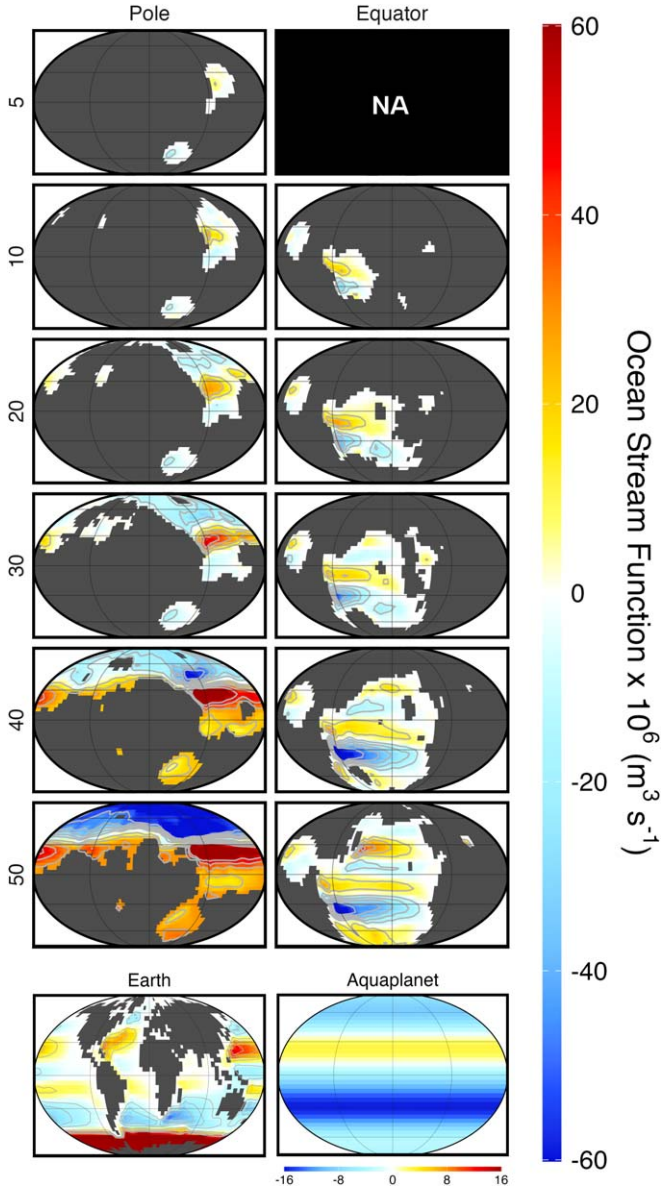

Figure 7. Ocean stream function for all WSAs (rows) and both continental orientations (columns). The topography of the equator-centered simulations (right column) has been rotated by 180° compared to similar plots above to center the map on the ocean and better show the ocean dynamics. Earth and aquaplanet control simulations are shown on the bottom left and right, respectively, for comparison. By convention, positive stream function values indicate clockwise flow. Note the change in scale for the aquaplanet simulation, where the stream function values are $\times 10^8$ m^3 s^{-1}. The E.2 simulation (equator-centered, 5% WSA) is not shown because this simulation was run using a lake model configuration, which is not capable of horizontal transport (see Section 2.2).

simulation (P.3). The E.3 simulation, however, has a substantially cooler climate, despite less radiative cooling from clouds. This difference in clouds is likely explained by an offsetting effect from ground albedo, as E.3 has the highest ground albedo of all simulations (Figure 3(B)).

The Arrakis-like simulations have minimal cloud$_{net}$ simply due to a lack of clouds in general. The Arrakis-like simulations are water-limited, leading to decreased coverage in all types of clouds (Figure 4) and low mean atmospheric albedo (Figure 5 (middle panel)). The relatively high net cloud radiative effect, as well as decreased snow and ice coverage, causes notable warming in the Arrakis-like simulations.

4.2.3. Atmosphere and Ocean Circulation

Atmospheric circulation shows stark differences between continental orientations, particularly at lower (0%–30%) WSA (Figure 6). The pole-centered simulations show a strong northern Hadley cell and a weak or nonexistent southern Ferrel cell. The higher global surface temperatures and higher north pole temperatures are likely due in part to the strong northern Hadley cell in the pole-centered simulations. The equator-centered simulations, conversely, show Hadley cells that are more balanced and weaker in magnitude. The large north–south differences in the pole-centered simulations are likely due to the strong north–south dichotomy in topography (Figure 1), which produces reasonably strong north–south differences in surface temperature (Figure 2). The equator-centered simulations do not have a pronounced north–south dichotomy in topography and therefore have relatively balanced surface temperatures and Hadley cells. These results suggest that continental orientation affects atmospheric circulation, which has cascading effects on climate.

Continental orientation has large effects on ocean circulation, particularly at higher (40%–50%) WSA (Figure 7). These effects, similar to atmospheric circulation, stem from the topographic dichotomy and resulting continental orientation. The pole-oriented simulations have a latitudinally continuous ocean, which allows stronger circulation since there is no land to hinder flow. The 40% and 50% WSA, pole-centered simulations show similar circulation patterns as observed in Earth's Southern Ocean (Figure 7), where there is a latitudinally continuous ocean. The large magnitudes of ocean circulation in the 40% and 50% WSA, however, do not have measurable effects on any of the climatological variables investigated in this study. This suggests that continental orientation, compared to ocean circulation, has a larger effect on climate on land-dominated planets ($\leqslant$50% WSA).

5. Summary and Conclusion

Many exoplanet climate studies have focused on aquaplanet scenarios (i.e., planets with a global ocean). These aquaplanets may be habitable and have abundant liquid surface water, but there are several reasons to be skeptical of their ability to sustain life, including (i) a lack of bioessential nutrients (B. J. Foley 2015; D. M. Glaser et al. 2020; D. Höning & T. Spohn 2023), (ii) a lack of carbonate-silicate climate feedback (J. C. G. Walker et al. 1981; B. J. Foley 2015), and (iii) a reduced extent of circumstellar HZ (Y. Abe et al. 2011). Arid or land-dominated exoplanets have shown promise in sustaining habitable surface conditions (Y. Abe et al. 2011; T. Kodama et al. 2019; M. Turbet et al. 2022); however, simulating planets with a mixture of continents and oceans is difficult, as the inclusion of continents adds an additional parameter to investigate.

Here we describe an ensemble of climate simulations to assess the effect of (i) WSA and (ii) continental orientation on the T_{surf} of an Earth-sized, land-dominated planet with modern Earth's instellation and paleo-Mars's topography. Our results, with respect to WSA, are consistent with previous work that shows (i) a positive relationship between water inventory and T_{surf} at higher water inventories (M. Turbet et al. 2016; M. J. Way & A. D. Del Genio 2020) and (ii) a breakdown of this trend (increased T_{surf}) at the lowest water inventories (Y. Abe et al. 2011; A. D. Del Genio et al. 2019b; T. Kodama et al. 2019).

Our results show that continental orientation plays a measurable role in the climate of these land-dominated planets.

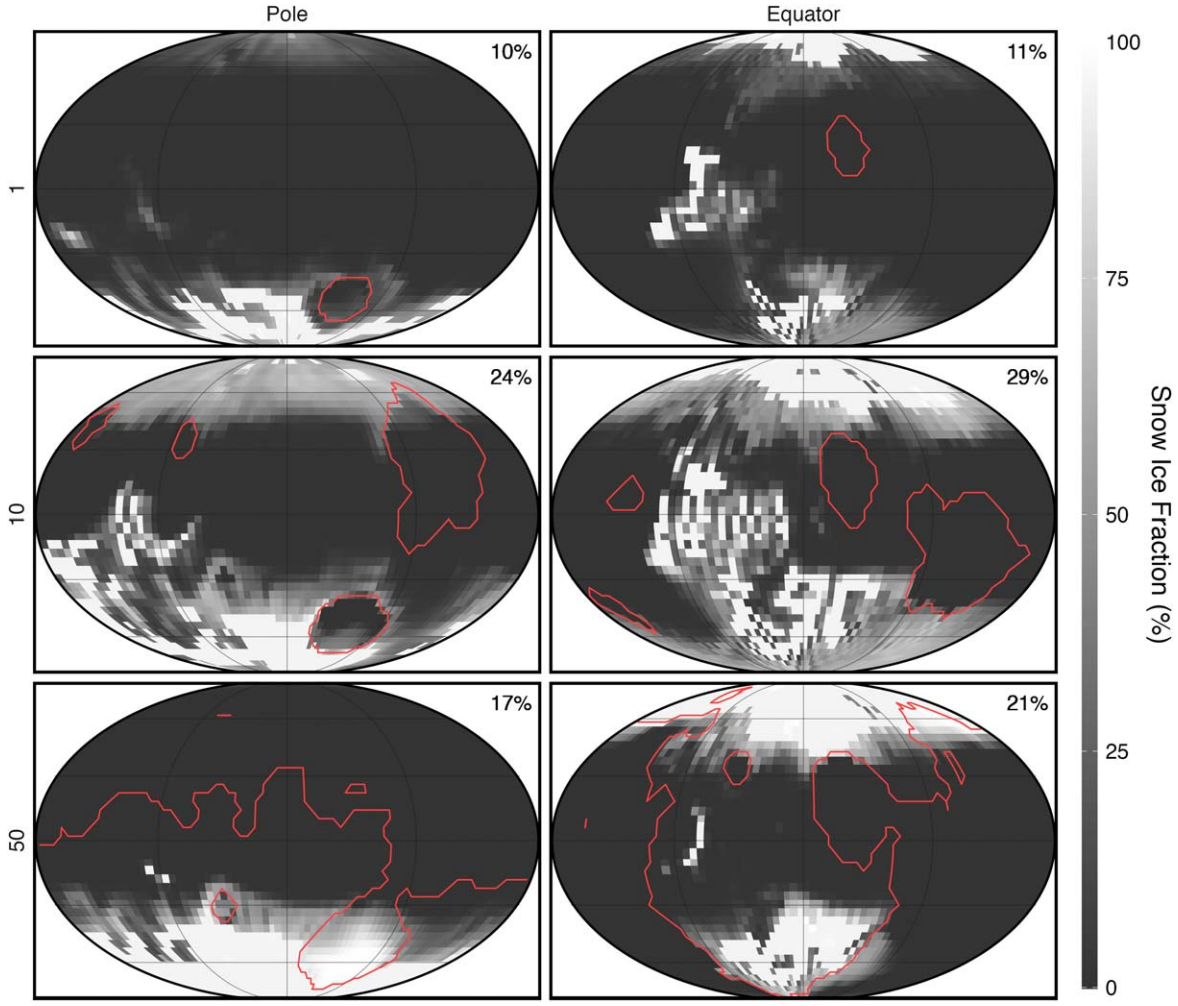

Figure 8. Equilibrium snow and ice fraction maps for the 1%, 10%, and 50% WSA (rows; top to bottom) simulations for the pole-centered (left) and equator-centered (right) orientations. Ice fraction includes land, lake, and sea ice. Values in the upper right of each panel are the global mean snow and ice fraction. The red lines are initial sea level, and latitude grid lines are shown at 0°, ±30°, and ±60°.

In general, planets with a pole-centered continental orientation are 3°C–5°C warmer, compared to the equator-centered planets (Figure 3(A)). This is due to two factors: (i) increased snow and ice coverage (Figure 3(C)) and (ii) lower net cloud radiative effects (Figure 5 (top panel)). Snow and ice cover is a cooling factor due to the high albedo of solid water, resulting in increased solar reflectance. The effects of clouds are more complex, however; lower $\text{cloud}_{\text{net}}$ values produce roughly 3 W m^{-2} of global cooling in the equator-centered simulations compared to pole-centered.

Our results show that the distribution of highlands is the primary factor controlling snow and ice deposition. The equator-centered simulations have highlands in the high latitudes of both poles. This allows yearlong snow and ice persistence, which reflects much of the solar radiation, especially in the summer months.

The cooling effect of continental distribution is reduced or almost eliminated for the driest, Arrakis-like, simulations (0% and 1% WSA). This extremely limited water inventory prevents widespread snow and ice deposition and cloud formation, since both processes require water. This lack of water decouples planetary albedo (encompassing snow and ice and clouds) from global mean T_{surf}. In other words, planetary albedo is a function of water inventory with a negative relationship from 5% to 100% WSA. However, at low WSA (0% and 1%), there is either a positive relationship or no correlation. The results of this study are insufficient to determine the relationship between planetary albedo and WSA in Arrakis-like planets; further research is needed.

This investigation continues the ongoing work of constraining the potential climate scenarios of HZ exoplanets as a function of an array of unobservable variables. Our ensemble of simulations has mean global T_{surf} values ranging from −1.°0C to 20.°5C (Figure 3(A)). These planets, all with the same instellation and atmosphere, have different (i) global mean temperatures, (ii) ground albedos, (iii) planetary albedos, (iv) cloud radiative effects, and (v) atmospheric circulation, which all serve to produce profoundly different climate states solely due to surface water inventory and continental orientation, both of which are currently unobservable on exoplanets. This highlights the importance of future missions such as HWO, which will attempt to image and characterize the surfaces of exoplanets. Surface imagery from HWO will prove to be of immeasurable value to further constrain the climate of potentially habitable planets in the search for life elsewhere.

Acknowledgments

The authors thank the two anonymous reviewers who provided excellent feedback, which served to vastly improve

this manuscript. D.M.G. was supported by the NASA Postdoctoral Program. M.J.W., A.I., and A.L. were supported by an award from the NASA Interdisciplinary Consortia for Astrobiology Research Program from the Planetary Science Division of the Science Mission Directorate. Resources supporting this work were provided by the NASA High-End Computing Program through the NASA Center for Climate Simulation at Goddard Space Flight Center. M.J.W. and I.A. acknowledge support from the GSFC Sellers Exoplanet Environments Collaboration (SEEC), which is funded by the NASA Planetary Science Division's Internal Scientist Funding Model. Thanks to Nancy Kiang, Reto Reudy, and the land surface model team at GISS for the help navigating the intricacies of the ROCKE-3D land planets configuration and their improvements to the lakes and hydrology modules used in this work. Thanks to Linda Sohl and Adrian Lenardic for the thoughtful input on the basis of planetary topography and the potential impacts on climate. Thank you to Jeffrey Jonas for invaluable input on topography transformation methods. D.M.G. thanks Ondrea Clarkson for answering the innumerable questions regarding the model and linux best practices. D.M.G. also sends a special thanks to the GISS early career group for much appreciated inspiration and support.

Data Availability

All model initialization files, raw model output, and reduced data can be downloaded from the open-access NASA NCCS data portal (https://portal.nccs.nasa.gov/GISS_modelE/ROCKE-3D/publication-supplements/Glaser2024PSJ-Continental_Distribution_and_the_Habitability_of_LandDominated_Arid_Planets) and on Zenodo (doi:10.5281/zenodo.14736289).

Software: The source code for ROCKE-3D, as well as installation and use instructions, is available from the NASA website at https://simplex.giss.nasa.gov/gcm/ROCKE-3D/.

Appendix A
Topography Transformation

Here we rotate the paleo-Mars topography by 90° ($\frac{\pi}{2}$ rad; ϕ) via a three-step process to create the "equator-centered" distribution. First, we convert from lat, lon (in radians) to x-, y-, z-coordinates:

$$x = \cos(\text{lon}) \times \cos(\text{lat}), \tag{A1}$$

$$y = \sin(\text{lon}) \times \cos(\text{lat}), \tag{A2}$$

$$z = \sin(\text{lat}). \tag{A3}$$

Then we rotate each cell by ϕ:

$$x' = (\cos(\phi) \times \cos(0) \times x) + (\sin(0) \times y) + (\sin(\phi) \times \cos(0) \times z), \tag{A4}$$

$$y' = (-\cos(\phi) \times \sin(0) \times x) + (\cos(0) \times y) - (\sin(\phi) \times \sin(0) \times z), \tag{A5}$$

$$z' = (-\sin(\phi) \times x) + (\cos(\phi) \times z). \tag{A6}$$

Lastly, we convert back to lat, lon coordinates:

$$\text{lat}' = \arcsin(z'), \tag{A7}$$

$$\text{lon}' = \begin{cases} \arctan\left(\frac{y'}{x'}\right); & \text{if } x' > 0 \\ \arctan\left(\frac{y'}{x'}\right) + \pi; & \text{if } x' < 0 \text{ and } y' \geqslant 0 \\ \arctan\left(\frac{y'}{x'}\right) - \pi; & \text{if } x' < 0 \text{ and } y' < 0 \\ \frac{\pi}{2}; & \text{if } x' = 0 \text{ and } y' > 0 \\ -\frac{\pi}{2}; & \text{if } x' = 0 \text{ and } y' < 0, \end{cases} \tag{A8}$$

to produce the final 90° TPW rotated topography.

Appendix B
Equilibrium Assessment

Each simulation was assessed for equilibrium conditions using the last 50 yr of global T_{surf}, Rad_{net}, Prec, and Evap_{pot} averages, as described in Section 2.4.2. The simulation is considered in equilibrium if the slope of the 50 yr subset is statistically similar to a line with a slope of 0. In addition, each simulation must have a Rad_{net} between −0.3 and 0.3 W m^{-2}. We do not consider the equilibrium time series for Earth, as we assessed equilibrium by matching historical observations.

Here we show the T_{surf}, Rad_{net}, Prec, and Evap_{pot} time series for the P.1 simulation (Figure 9).

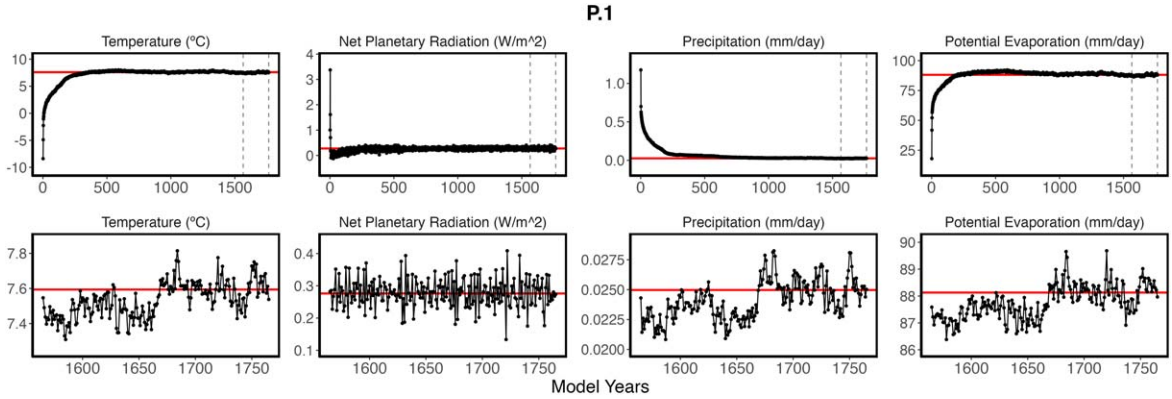

Figure 9. Time series of T_{surf} (first column), Rad_{net} (second column), Prec (third column), and Evap_{pot} (fourth column) for the P.1 simulation. Top panels are the entire 1765 yr of simulation, and bottom panels are a zoomed-in plot of the last 200 yr, shown by vertical dashed lines in the top panels. Red horizontal lines indicate the mean equilibrium value of the last 50 simulation yr.

(The complete figure set (17 images) is available in the online article.)

Appendix C
Net Planetary Radiation

Net planetary radiation as a function of WSA for all simulations is shown in Figure 10.

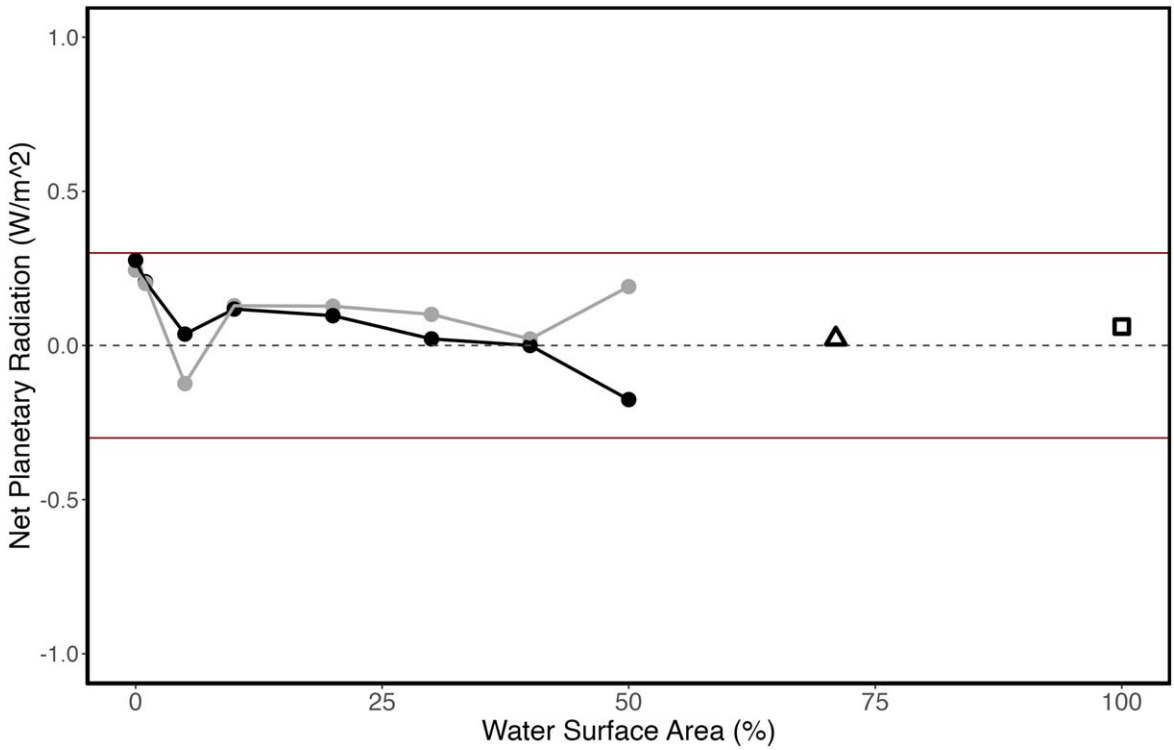

Figure 10. Equilibrium mean net planetary radiation as a function of WSA for the pole-centered (black) and equator-centered (gray) simulations. The black square is the control aquaplanet simulation, and the black triangle is modern Earth. A dashed gray line at 0 W m^{-2} is shown for reference. All simulations equilibrate between −0.3 and 0.3 W m^{-2} (red lines), suggesting stable climate conditions.

Appendix D
Cloud Spatial and Vertical Variability

The spatial and vertical distribution of clouds observed here is complex. In general, the clouds tend to persist over land and the poles in all simulations (Figure 11). Increased WSA increases the extent of clouds but only in a stepwise way between 1% and 5% WSA (Figure 4), and all simulations between 5% and 100% have similar total cloud coverage (∼55%). Increased WSA does not change the distribution of clouds (Figure 11). Similarly, changes in continent orientation do not change the extent of clouds (see Figure 4), but the change in orientation does have an effect on the distribution of clouds (Figure 11).

The vertical extent and distribution of clouds, however, do show changes as a function of both WSA and continental orientation (Figure 12). In general, the thickness (vertical extent) of the low and midclouds increases with increasing WSA, especially in the higher latitudes. The equator-centered simulations show a roughly even distribution of low clouds in the higher latitudes compared to the pole-centered simulations, where the north pole has thinner clouds, especially at higher WSA (Figure 12).

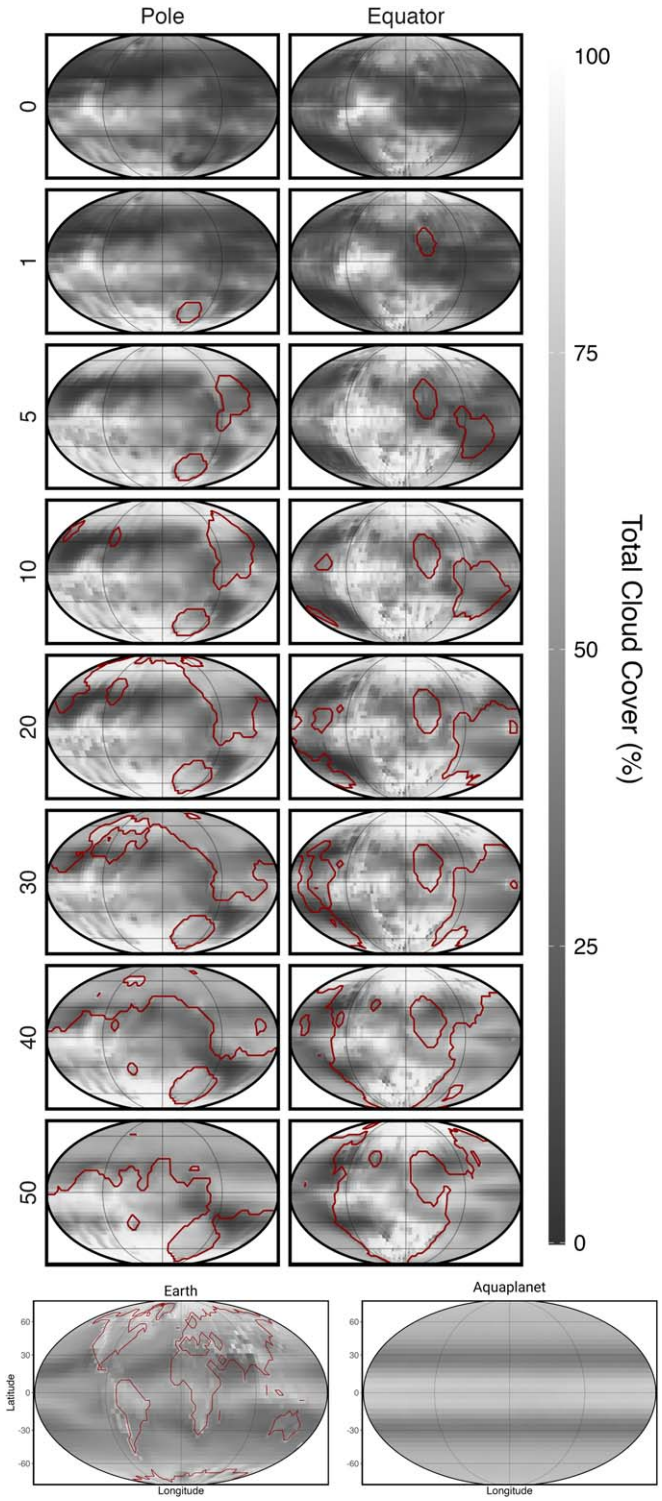

Figure 11. Equilibrium mean total cloud cover maps as a function of WSA (rows) for the pole-centered (left column) and equator-centered (right column) simulations. The dark red lines are initial sea level, separating land from ocean/lake. Latitude grid lines are shown at 0°, ±30°, and ±60°.

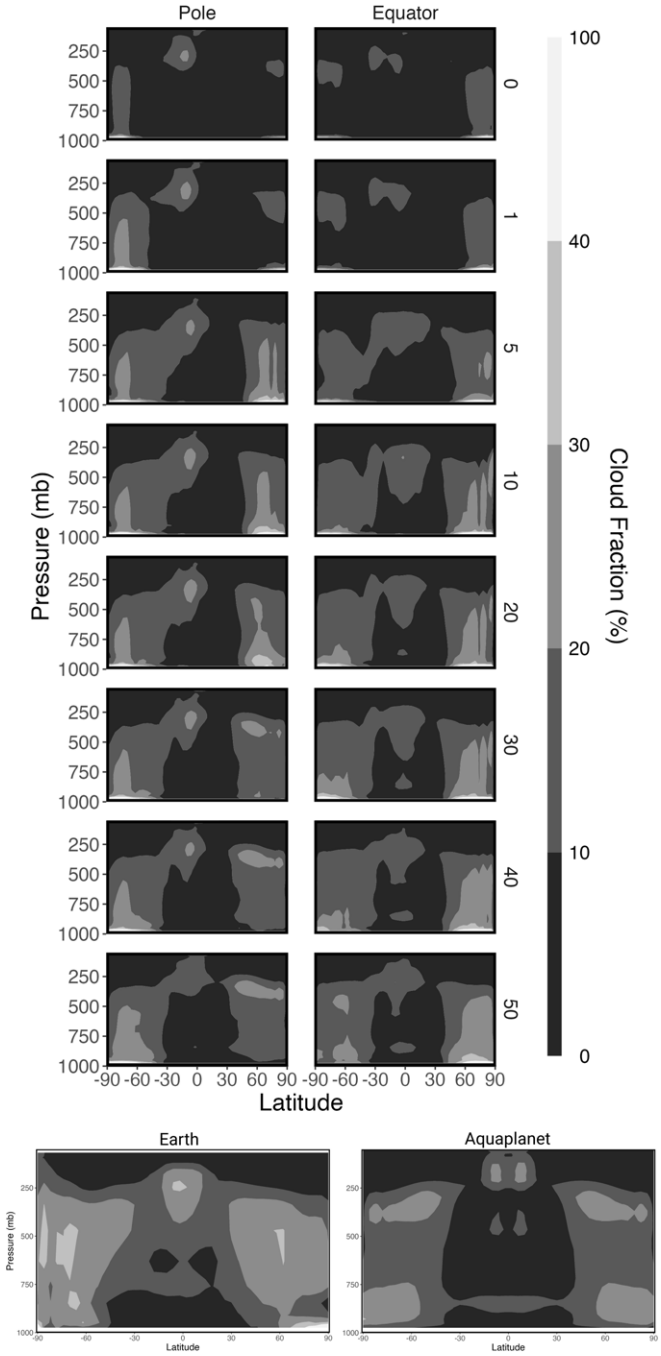

Figure 12. Equilibrium mean zonal (latitudinal average; *x*-axis) cloud fraction vs. pressure (*y*-axis) as a function of WSA (rows) for the pole-centered (left column) and equator-centered (right column) simulations. Note that the brightest color indicates cloud fraction values greater than 40%.

Appendix E
Precipitation

Precipitation scales linearly with WSA in these simulations for both continental orientations (Figure 13). The equator-centered simulations show slightly higher precipitation in all simulations except for 5% WSA. This is likely due to the extended region of low precipitation between 0° and 30°N in the pole-centered simulations (Figure 14, left column). The dry interior observed in the pole-centered simulations between 0% and 40% WSA is an example of an effect of climate from continental orientation. Precipitation, similar to many of the other variables (e.g., surface temperature, ground albedo, and snow and ice coverage), shows a steplike change with increased WSA. The two continental orientations show different patterns in precipitation distribution (Figure 14). Precipitation locates in the equator of both orientations, but the main spatial difference is the precipitation in the highlands, which is distributed differently in the two orientations.

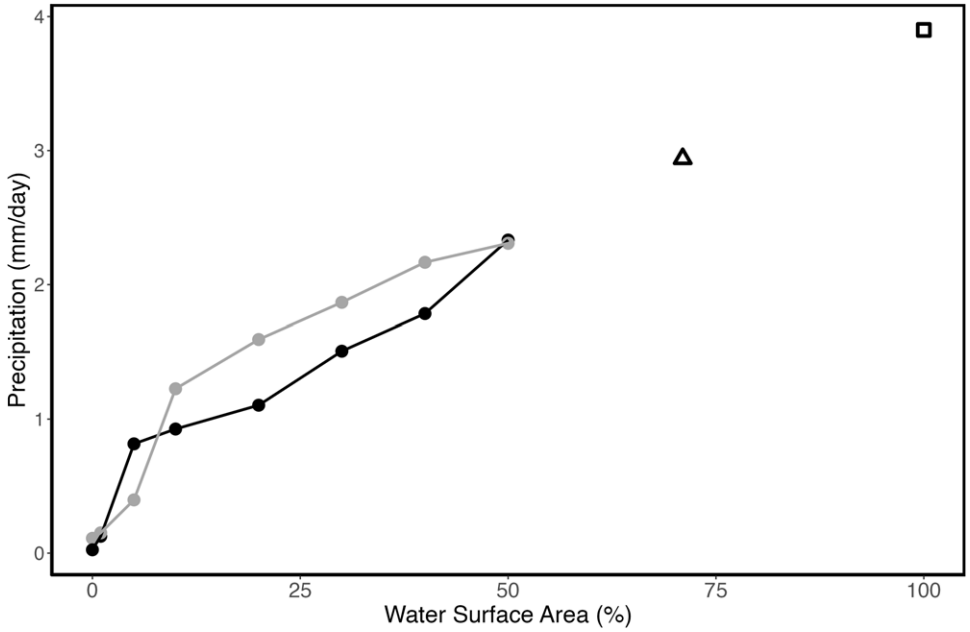

Figure 13. Equilibrium mean global precipitation for the pole-centered (black) and equator-centered (gray) simulations. The black square is the control aquaplanet simulation, and the black triangle is modern Earth.

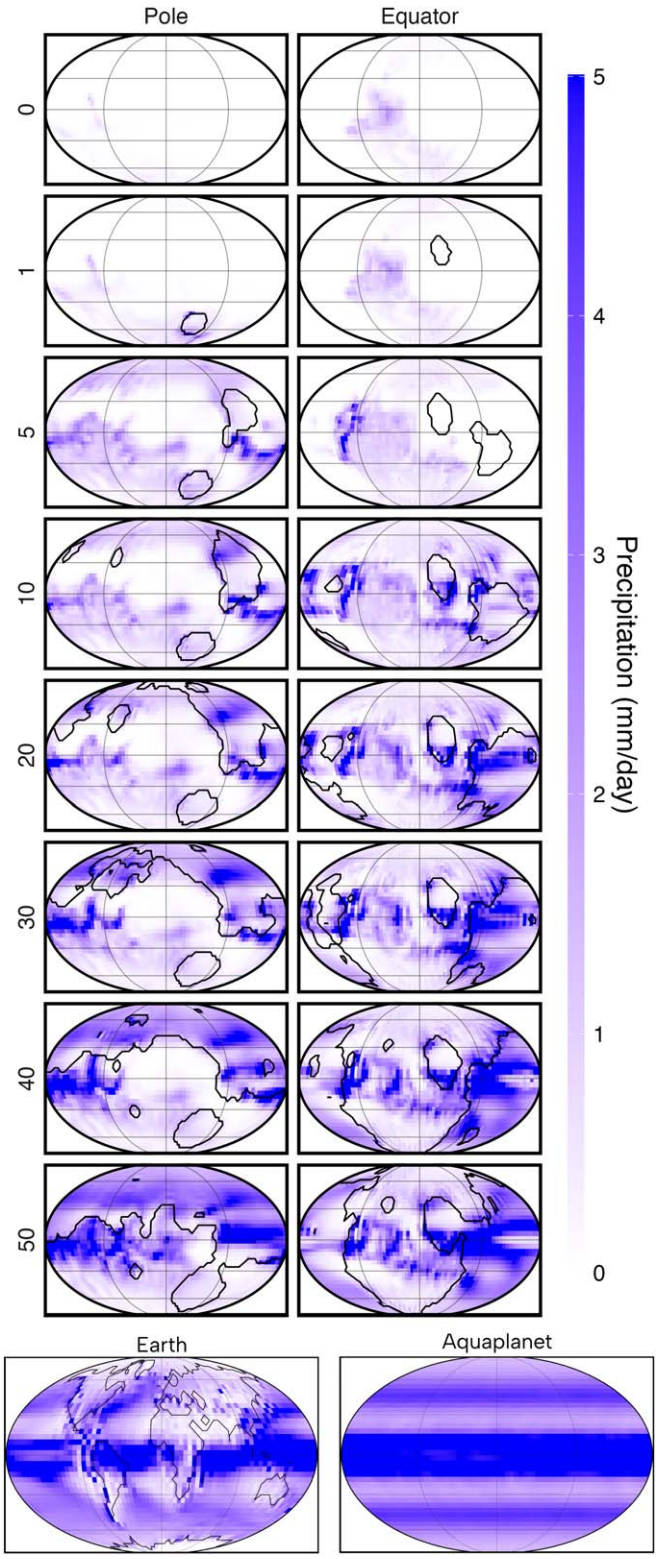

Figure 14. Equilibrium mean precipitation maps as a function of WSA (rows) for the pole-centered (left column) and equator-centered (right column) simulations. The black lines are initial sea level, separating land from ocean/lake. Latitude grid lines are shown at 0°, ±30°, and ±60°.

Appendix F
Low Water Inventory Simulations

The low water abundance simulations tended to completely evaporate their initial water bodies (Hellas Basin), leading to a fatal model crash. To investigate these low water inventory scenarios, it was necessary to initialize these water bodies as lakes, as opposed to oceans, which are able to fully evaporate in the simulations. There are two main differences in the model between ocean and lakes. First, the ocean cells in ROCKE-3D are dynamic, meaning that they have lateral heat transport between grid cells. Dynamic oceans, compared to "slab" oceans, are able to realistically distribute heat. This is especially important where

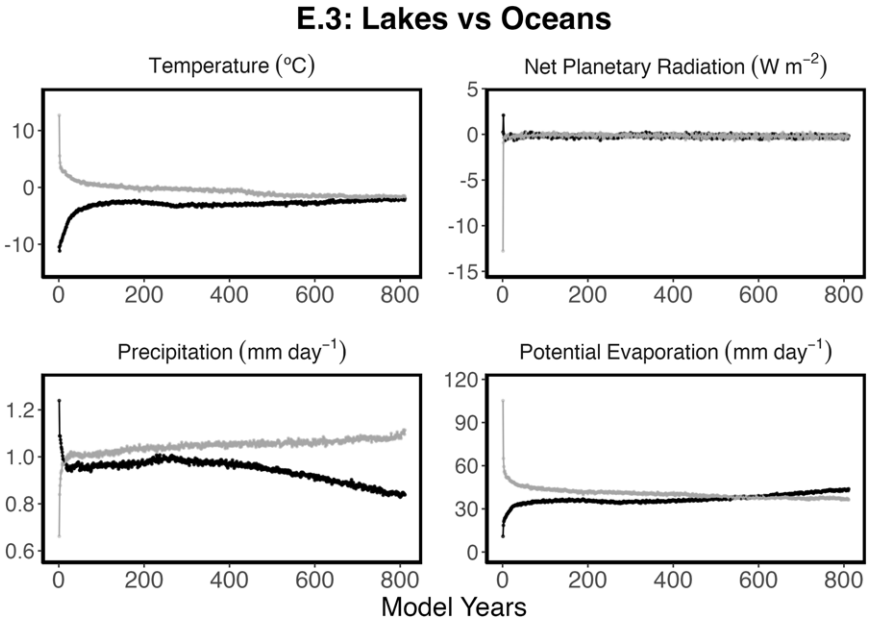

Figure 15. Equilibrium temperature (top left), net planetary radiation (top right), precipitation (bottom left), and potential evaporation (bottom right) time series for simulation E.3 using the ocean (gray) and lake (black) model configurations.

there are latitudinal, contiguous expanses of oceans as in the pole-centered configurations with 30% or more WSA (P.6, P.7, and P.8). Lastly, the ocean and lake cells have different salinity: 0.035 kg kg^{-1} and 0 kg kg^{-1}, respectively.

While these differences may seem significant, we show that the final equilibrium state is likely similar between the ocean and lake simulations. Comparison of the lake and ocean simulations (Figure 15) shows that the climatalogical variables, T_{surf} and Rad_{net}, converge to the same value at the time of the ocean simulation crash. The hydrological variables, Prec and $Evap_{pot}$, may show some differences. The lake and ocean simulations approach similar $Evap_{pot}$ values: 44 and 36 mm day^{-1}, respectively. There is, however, a marked difference in Prec between the lake and ocean simulations. This may indicate different equilibrium values between the two simulations; however, hydrological variables (particularly in low water inventory simulations) take many model years to equilibrate. It seems as if the Prec values diverge, but it is likely that the global mean value in the ocean run is on the verge of peaking, then dropping, similar to the lake run. This is because the model crashed right before the ocean dried up. Once the ocean dries up, Prec is likely to trend downward, as seen in the lake simulation (Figure 15; lower left).

Appendix G
Model Diagnostic Names

Reference table for all variables of interest (Table 4).

Table 4
Reference Table for Variables Used in This Paper and Their Corresponding Names in the Model Output, If Applicable

Common Name	Paper Mathematical Variable	Model Diagnostic Name
Planetary albedo	α_{planet}	plan_alb
Ground albedo	α_{ground}	grnd_alb
Longwave cloud reemission (TOA)	$cloud_{lw}$	lwcrf_toa
Shortwave cloud reflection (TOA)	$cloud_{sw}$	swcrf_toa
Surface temperature	T_{surf}	tsurf
Incident shortwave radiation (TOA)	Rad_{inc}	incsw_toa
Outgoing longwave radiation (TOA)	Rad_{out}	trnf_toa
Precipitation	Prec	prec
Potential evaporation	$Evap_{pot}$	pot_evap
Snow and ice coverage	⋯	snowicefr
Total cloud coverage	⋯	pcldt
Low cloud coverage	⋯	pcldl
Midcloud coverage	⋯	pcldm
High cloud coverage	⋯	pcldh
Stream function	⋯	psi_cp[a]
Ocean stream function	⋯	osfij[a]
Zonal cloud fraction	⋯	cf[a]

Note.
[a] All model diagnostics can be found in the .aij output files, except psi_cp (.agc), osfij (.oij), and cf (.aijl).

ORCID iDs

Donald M. Glaser https://orcid.org/0000-0002-1150-4605
Igor Aleinov https://orcid.org/0000-0002-7827-228X
Anthony Leboissetier https://orcid.org/0000-0001-9685-7815
M. J. Way https://orcid.org/0000-0003-3728-0475

References

Abe, Y., Abe-Ouchi, A., Sleep, N. H., & Zahnle, K. J. 2011, AsBio, 11, 443
Aleinov, I., & Schmidt, G. 2006, GPC, 51, 108
Anglada-Escudé, G., Amado, P. J., Barnes, J., et al. 2016, Natur, 536, 437
Astudillo-Defru, N., Forveille, T., Bonfils, X., et al. 2017, A&A, 602, A88
Barnes, R. 2017, CeMDA, 129, 509
Baumeister, P., & Tosi, N. 2023, A&A, 676, A106
Bouley, S., Baratoux, D., Matsuyama, I., et al. 2016, Natur, 531, 344
Clogg, C. C., Petkova, E., & Haritou, A. 1995, Am. J. Sociol., 100, 1261
Cockell, C. S., Simons, M., Castillo-Rogez, J., et al. 2024, NatAs, 8, 30
Del Genio, A. D., Way, M. J., Amundsen, D. S., et al. 2019a, AsBio, 19, 99
Del Genio, A. D., Way, M. J., Kiang, N. Y., et al. 2019b, ApJ, 887, 197
Delrez, L., Murray, C. A., Pozuelos, F. J., et al. 2022, A&A, 667, A59
Donohoe, A., & Battisti, D. S. 2011, JCli, 24, 4402
Dorn, C., Bower, D. J., & Rozel, A. 2018, in Handbook of Exoplanets, ed. H. J. Deeg & J. A. Belmonte (Berlin: Springer), 3111
Dorn, C., & Lichtenberg, T. 2021, ApJL, 922, L4
Edwards, J. M. 1996, JAtS, 53, 1921
Edwards, J. M., & Slingo, A. 1996, QJRMS, 122, 689
Fauchez, T. J., Turbet, M., Wolf, E. T., et al. 2020, GMD, 13, 707
Foley, B. J. 2015, ApJ, 812, 36
Galuzzo, D., Cagnazzo, C., Berrilli, F., Fierli, F., & Giovannelli, L. 2021, ApJ, 909, 191
Gilbert, E. A., Barclay, T., Schlieder, J. E., et al. 2020, AJ, 160, 116
Gillon, M., Triaud, A. H. M. J., Demory, B.-O., et al. 2017, Natur, 542, 456
Glaser, D. M., Hartnett, H. E., Desch, S. J., et al. 2020, ApJ, 893, 163
Glaser, D. M., Hartnett, H. E., Finn, D. R., et al. 2022, AsBio, 22, 1222
Grimm, S. L., Demory, B.-O., Gillon, M., et al. 2018, A&A, 613, A68
Guimond, C. M., Shorttle, O., & Rudge, J. F. 2023, MNRAS, 521, 2535
Guzewich, S. D., Way, M. J., Aleinov, I., et al. 2021, JGRE, 126, e2021JE006825
Harada, C. K., Dressing, C. D., Kane, S. R., & Ardestani, B. A. 2024, ApJS, 272, 30
Höning, D., & Spohn, T. 2023, AsBio, 23, 372
Iyer, A. R., & Line, M. R. 2020, ApJ, 889, 78
Jiang, J. H., Zhai, A. J., Herman, J., et al. 2018, AJ, 156, 26
Kane, S. R., Arney, G., Crisp, D., et al. 2019, JGRE, 124, 2015
Kasting, J. F., & Catling, D. 2003, ARA&A, 41, 429
Kodama, T., Genda, H., Leconte, J., & Abe-Ouchi, A. 2021, JGRE, 126, e2021JE006975
Kodama, T., Genda, H., O'ishi, R., Abe-Ouchi, A., & Abe, Y. 2019, JGRE, 124, 2306
Koll, D. D. B., & Abbot, D. S. 2016, ApJ, 825, 99
Kopparapu, R. K., Wolf, E. T., Arney, G., et al. 2017, ApJ, 845, 5
Kossakowski, D., Kürster, M., Trifonov, T., et al. 2023, A&A, 670, A84
Labonté, M.-P., & Merlis, T. M. 2020, ApJ, 896, 31
Leconte, J., Forget, F., Charnay, B., et al. 2013, A&A, 554, A69
Lewis, N. T., Lambert, F. H., Boutle, I. A., et al. 2018, ApJ, 854, 171
Lobo, A. H., Shields, A. L., Palubski, I. Z., & Wolf, E. 2023, ApJ, 945, 161
Luger, R., & Barnes, R. 2015, AsBio, 15, 119
Macdonald, E., Paradise, A., Menou, K., & Lee, C. 2022, MNRAS, 513, 2761
Maruyama, S., Ikoma, M., Genda, H., et al. 2013, GeoFr, 4, 141
Menou, K. 2013, ApJ, 774, 51
National Academies of Sciences, Engineering, and Medicine 2021, Pathways to Discovery in Astronomy and Astrophysics for the 2020s (Washington, DC: National Academies Press)
Noack, L., Snellen, I., & Rauer, H. 2017, SSRv, 212, 877
O'Brien, D. P., Izidoro, A., Jacobson, S. A., Raymond, S. N., & Rubie, D. C. 2018, SSRv, 214, 47
Rackham, B. V., Apai, D., & Giampapa, M. S. 2018, ApJ, 853, 122
Ramirez, R. M., & Kaltenegger, L. 2014, ApJL, 797, L25
Raymond, S. N., Quinn, T., & Lunine, J. I. 2007, AsBio, 7, 66
Rushby, A. J., Shields, A. L., Wolf, E. T., Laguë, M., & Burgasser, A. 2020, ApJ, 904, 124
Salazar, A. M., Olson, S. L., Komacek, T. D., Stephens, H., & Abbot, D. S. 2020, ApJL, 896, L16
Sergeev, D. E., Lewis, N. T., Lambert, F. H., et al. 2022, PSJ, 3, 214
Shkuratov, Y., Kaydash, V., Korokhin, V., et al. 2011, P&SS, 59, 1326
Stephens, G. L., O'Brien, D., Webster, P. J., et al. 2015, RvGeo, 53, 141
Styczinski, M., Cooper, Z., Glaser, D., et al. 2024, AsBio, 24, S
Suárez Mascareño, A., González-Álvarez, E., Zapatero Osorio, M. R., et al. 2023, A&A, 670, A5
Tian, F., & Ida, S. 2015, NatGe, 8, 177
Tsigaridis, K., Ackerman, A. S., Aleinov, I., et al. 2025, GMD, submitted
Turbet, M., Fauchez, T. J., Sergeev, D. E., et al. 2022, PSJ, 3, 211
Turbet, M., Leconte, J., Selsis, F., et al. 2016, A&A, 596, A112
Unterborn, C. T., Desch, S. J., Hinkel, N. R., & Lorenzo, A. 2018, NatAs, 2, 297
Venturini, J., Ronco, M. P., & Guilera, O. M. 2020, SSRv, 216, 86
Vincendon, M., Audouard, J., Altieri, F., & Ody, A. 2015, Icar, 251, 145
Walker, J. C. G., Hays, P. B., & Kasting, J. F. 1981, JGR, 86, 9776
Way, M. J., Aleinov, I., Amundsen, D. S., et al. 2017, ApJS, 231, 12
Way, M. J., Davies, H. S., Duarte, J. C., & Green, J. A. M. 2021, GGG, 22, e2021GC009983
Way, M. J., & Del Genio, A. D. 2020, JGRE, 125, e2019JE006276
Yang, J., Leconte, J., Wolf, E. T., et al. 2019, ApJ, 875, 46
Zain, P. S., De Elía, G. C., Ronco, M. P., & Guilera, O. M. 2018, A&A, 609, A76
Zhao, Z., Liu, Y., Li, W., Liu, H., & Man, K. 2021, ApJL, 910, L8